Multiscale 3D displacement field measurement using stereo digital image correlation on a fractal speckle pattern

Joël Serra, R. Lalanne, John-Eric Dufour, Jean-Noël Périé, Jean-Charles Passieux

▶ **To cite this version:**

Joël Serra, R. Lalanne, John-Eric Dufour, Jean-Noël Périé, Jean-Charles Passieux. Multiscale 3D displacement field measurement using stereo digital image correlation on a fractal speckle pattern. Strain, 2024, pp.e12479. 10.1111/str.12479 . hal-04586145

HAL Id: hal-04586145

https://insa-toulouse.hal.science/hal-04586145v1

Submitted on 24 May 2024

HAL is a multi-disciplinary open access archive for the deposit and dissemination of scientific research documents, whether they are published or not. The documents may come from teaching and research institutions in France or abroad, or from public or private research centers.

L'archive ouverte pluridisciplinaire **HAL**, est destinée au dépôt et à la diffusion de documents scientifiques de niveau recherche, publiés ou non, émanant des établissements d'enseignement et de recherche français ou étrangers, des laboratoires publics ou privés.

Check for updates

Received: 20 July 2023 | Revised: 24 April 2024 | Accepted: 2 May 2024

DOI: 10.1111/str.12479

RESEARCH ARTICLE

strain WILEY

Multiscale 3D displacement field measurement using stereo digital image correlation on a fractal speckle pattern

J. Serra | **R. Lalanne** | **J.-E. Dufour** | **J.-N. Périé** | **J.-C. Passieux**

Université de Toulouse, Institut Clément Ader, ISAE-SUPAERO – UPS – IMT Mines Albi – INSA, Toulouse, France

Correspondence
J. Serra, Université de Toulouse, Institut Clément Ader, ISAE-SUPAERO – UPS – IMT Mines Albi – INSA, Toulouse, France.
Email: joel.serra@isae-supaero.fr

Funding information
Fondation Lopez Loreta, Grant/Award Number: Prix Lopez Loreta 2018

Abstract

Even though the simulations used to predict failure are becoming increasingly predictive, complex multiaxial loading tests are still required to validate the design of structural components in a wide range of industries. Large specimen testing often requires two different scales. A global *Far Field* to obtain boundary conditions and a local *Near Field* to evaluate strain gradients around discontinuities such as bolts, notches... The main goal of this study is to provide a continuous displacement over the whole specimen surface integrating data from multiple cameras. In this paper, we propose a new methodology that generates 3D displacements determined by finite-element stereo digital image correlation in the *Near Field* and in the *Far Field* using a unique fractal speckle pattern and an off-line determined *texture*. The displacements are obtained in the same coordinate system and on the same mesh. Satisfactory data fusion from both *Near Field* and *Far Field* images of a biaxial test on a notched laminate composite was obtained with a refined mesh at the notch tip. This methodology can be applied to any tests requiring multiple camera systems and will support the use of the finite-element digital image correlation framework as an experimental-numerical efficient technique.

KEYWORDS

camera cluster calibration, fractal speckle, multiscale, near-field/far-field measurement, stereo digital image correlation

1 | INTRODUCTION

Composite structures are now widely used in most transportation vehicles, especially in the aerospace and astronautics fields [1]. In practice, the development and certification of these structures is still based on experimental validations in an approach known as the 'test pyramid', originally developed by Rouchon [2]. The concept has also been used in other fields such as automotive engineering [3] or wind turbines. The base of the pyramid, at the coupon level, enables allowable values and their scatter to be obtained. Tests are performed on coupons under uniaxial loading. The upper levels of the pyramid enable model validation. These resort to much more complex tests on specimens that are increasingly close in shape and size to the final design of the various parts. The complexity of these tests gives rise to two major issues.

This is an open access article under the terms of the Creative Commons Attribution-NonCommercial License, which permits use, distribution and reproduction in any medium, provided the original work is properly cited and is not used for commercial purposes.
© 2024 The Authors. *Strain* published by John Wiley & Sons Ltd.

First, unlike uniaxial coupon testing, the stress state resulting from the displacement/force applied by the remote actuators cannot be accurately determined in most cases. In fact, the redundancy of the load paths and the dependence of the test machine stiffness on the specimen under test make it difficult to have a transfer function that would relate the actuator displacement to the actual boundary conditions applied to the specimen. It is therefore necessary to monitor the test in situ in order to identify them. Strain gages have long been the primary means of monitoring structural tests. Indeed, the use of such high-resolution sensors judiciously placed around the region of interest (ROI) in a region that remained sound (test body) enabled the actual load and moment fluxes applied to the specimen to be estimated [4]. The emergence of stereo digital image correlation (SDIC) methods helped greatly with these issues with 3D displacements that can now be measured on the surface of the specimen over time [5]. Digital image correlation is based on the premise that changes in the image grey levels result from the mechanical transformation of the observed object. Traditionally, DIC techniques involve minimizing a parameter that measures the difference between the grayscale values in the original (undeformed) image and the deformed image. DIC methods generally fall into two main categories: subset-based methods, also known as local approaches, involve searching for displacements as piecewise polynomials (often linear or quadratic) within a set of small, typically square, subsets of the entire ROI, leading to a large amount of small and independent problems. Conversely, global approaches seek the displacement as a linear combination of globally defined shape functions (usually finite elements [FEs], splines, closed forms ...). The minimization of the criteria across the entire ROI simultaneously leads to one single but larger problem.

Second, when instrumenting a large structure, multiple cameras are often required to achieve the desired measurement resolution at a given scale [6–8]. For example, consider an extreme case such as the inspection of 50-m-long wind turbine blades [7]. It is clearly impossible to capture a displacement gradient under the chord scale with a single stereo camera rig that would film the entire blade. Therefore, several systems are used along the blade's span. For very specific cases, such as mode shape determination, a single stereo camera rig can be used and moved along the structure to capture images of different sections. The global structural mode shape has to be reconstructed in a post-processing step, using a complex stitching of the independent stereo measurements [9]. When structural details are expected to occur, a multiscale analysis might be preferred. In practice, instead of paving the space with a multitude of stereo camera rigs of equivalent optical resolution [8], one can imagine adding higher resolution images in regions where higher gradients are expected [10–12]. In the present study, the far-field (FF) is required to provide access to the global behaviour of the specimen and the near-field (NF) is needed to obtain accurate displacement gradients around the notch. However, such multiscale measurements come with calibration and data merging issues [13].

The relative positioning of multiple stereo rigs must be estimated. A calibration step is thus required. This problem has been addressed in the literature. Several methods have been identified to position the NF camera rig relative to the FF one. Natural features can be used as identifiable references that can be seen from the multiple points of view. For example, the crack and its tip can be used to determine the relative positioning of the two cameras [14–16]. Artificial features that are visible from all cameras can also be used. They are usually encoded in the speckle, as in the work of Shao et al. [17]. They can also take the form of marks deposited by the experimenter [18]. In the vision community, the construction of dynamic systems composed of FF cameras and very narrow views enables 'gigapixels' imaging systems to be built by stitching them together [19]. These different methods rely on the detection of common features in images acquired at different scales. Some of these features might be extracted manually, but most of the information can be identified automatically using feature detection algorithms such as scale invariant feature transform (SIFT) [20] or speeded up robust features (SURF) [21]. The calculation of the relative positioning of the different cameras with respect to each other can then be computed from the knowledge of the feature positions using classical bundle adjustment methods [22]. Local correlation approaches, that consider disconnected subset independently [23], can perform either geometric or photometric stitching [24]. To estimate the rigid transformation between two 3D point clouds, the geometric stitching method uses 3D corresponding points, and the photometric ones use 2D ones (in the images). Both are available for instance in VIC 3D © [25]. Up to now, the merging of several 3D DIC displacement fields (NF and FF for example) was usually performed with extra stitching steps (interpolation of overlapping data) [13, 26]. Instead, a priori calibration classic to FE-DSIC is used here to position all the cameras relative to a unique mesh. A multiview calibration formulation, as proposed in previous works [15, 16, 27], was used with a reference texture [14]. A dedicated solution algorithm, using SIFT as an initial guess following other works [12, 28], is proposed to perform this multiscale calibration.

So far, in all the cited literature, the techniques look more like a juxtaposition and a posteriori stitching of multiple classical DIC measurements. In contrast, a true multiscale SDIC approach is proposed here. Recent global correlation approaches are formulated as a grey level conservation problem in the world coordinate system [27, 29] that seems

14751305, 0, Downloaded from https://onlinelibrary.wiley.com/doi/10.1111/str.12479 by Cochrane France, Wiley Online Library on [23/05/2024]. See the Terms and Conditions (https://onlinelibrary.wiley.com/terms-and-conditions) on Wiley Online Library for rules of use; OA articles are governed by the applicable Creative Commons License

more appropriate for such multiscale data assimilation DIC than subset-based methods. More specifically, FE-SDIC [27] was used in this study. In FE-SDIC, the same FE mesh can be used for both the measurement of the 3D displacement field and the numerical simulation. This allows for a very convenient coupling of simulations and measurements (boundary conditions assessment, direct comparisons of nodal displacement fields, etc.). But the main advantage here, is that, once the different cameras are positioned relative to a mutual reference (i.e., the mesh coordinate system), the displacement measurement (defined on the whole entire surface of the specimen), can be performed from all the cameras regardless of their scales or positions. In a 2D configuration, Passieux et al. used homographic functions to relate NF to FF data [12]. They initialized their algorithm with matched points between the two fields of view using a SIFT algorithm [20]. On the same 2D dataset, Bouclier and Passieux were able to couple NF and FF mechanically regularized measurements using Lagrange multipliers [30]. Both methods allowed the computation of a continuous displacement solution defined on a unique mesh taking advantage of both NF and FF images, but they were (1) limited to 2D configurations and (2) did not use all the available images because the FF images were not used in the NF region.

The proposed multiscale DIC framework uses all the available images to improve the measured kinematic fields. In other words, to compute the displacement at one point (in the FE mesh), all the grey levels of all available images are used to estimate the displacement. This means that the same region is measured from cameras with possibly very different resolutions. The question of the speckle pattern scale is therefore central. The measurement resolution in DIC is related to the pattern feature size. The latter should be carefully chosen to achieve the target resolution. More precisely, the Good Practices Guide of iDICs [31] recommends an ideal pattern feature size of 3–5 pixels. However, in a multiscale context, a pattern optimized for the NF is likely to be too fine for the FF. For a two-scale analysis, Bomarito et al. [32] first proposed an interesting technique to generate a two-scale pattern. In this work, for the sake of genericity, a so-called fractal speckle [33] was used. This pattern, which has been theoretically shown to be scale invariant, was used and experimentally tested here for the first time.

This paper presents an alternative Multi-SDIC approach. No additional stitching step is required to obtain a continuous displacement over the entire specimen surface integrating data from all cameras. In the context of large-scale testing, the originality of this work resides in (i) a new multiscale SDIC framework; (ii) a specific calibration procedure based on a multicamera grey level formulation with an initial guess build using a scale invariant template matching algorithm; (iii) a generic fractal speckle pattern. The 3D displacements determined by FE-SDIC in the NF and in the FF are therefore obtained in the same coordinate system and on the same (refined near-notch) mesh.

The paper is organized as follows. The experimental setup is described in Section 2.1. In Section 2.2, the scale invariant properties of the fractal pattern are assessed experimentally. In Section 3.1, some basics of FE-SDIC are recalled. Then, Section 3.2 presents the new calibration procedure, and the multiscale SDIC displacement technique is detailed in Section 3.3. The conclusion and discussion are detailed in Section 4.

2 | EXPERIMENTAL TEST CASE

2.1 | VERTEX test bench description and material

The experimental test bench used in this work (Figure 1) has been developed by Castanié [4] and first used by Serra et al. at the Institut Clément Ader in 2014 [15, 34].

The specimen is bolted to the upper surface of the centre box structure with 128 fasteners. Once bolted, the remaining ROI is 400 × 400 mm^2. The actuators are driven in displacement control. When actuators 1 and 2 apply a vertical load, the central box is subjected to bending, and the plate (top facet of the central box) is loaded in compression or tension. When actuators 3 and 4 are activated, the centre box is subjected to torsion, and the plate is loaded in shear.

As underlined by Serra et al. [15, 35, 36], one difficulty with this test method is accurately assessing the plate forces and moments distributions applied to the specimen. Because of numerous structural redundancies (hyperstatism) of the test rig and the dependency of the test rig stiffness to the stiffness of the tested specimen, it is not easy to know the transfer function that links actuator forces to fluxes actually entering the specimen. Therefore, an in situ measurement is needed. The authors opted for SDIC using several stereo camera rigs (Figures 1—bottom and 2). Two 29MPx cameras are used to create the required 'intrinsic' texture (Section 3.2). They are not used to perform real-time monitoring of the test due to limited bandwidth (<29MPx/s), storage and computation issues. Two 5 MPx camera stereo rigs are rather used to record, respectively, (i) FF images of the specimen and (ii) NF images of a notch end. The aim is to obtain, respectively, (i) the global behaviour of the specimen and (ii) an accurate displacement field in the high stress

14751305, 0, Downloaded from https://onlinelibrary.wiley.com/doi/10.1111/str.12479 by Cochrane France, Wiley Online Library on [23/05/2024]. See the Terms and Conditions (https://onlinelibrary.wiley.com/terms-and-conditions) on Wiley Online Library for rules of use; OA articles are governed by the applicable Creative Commons License

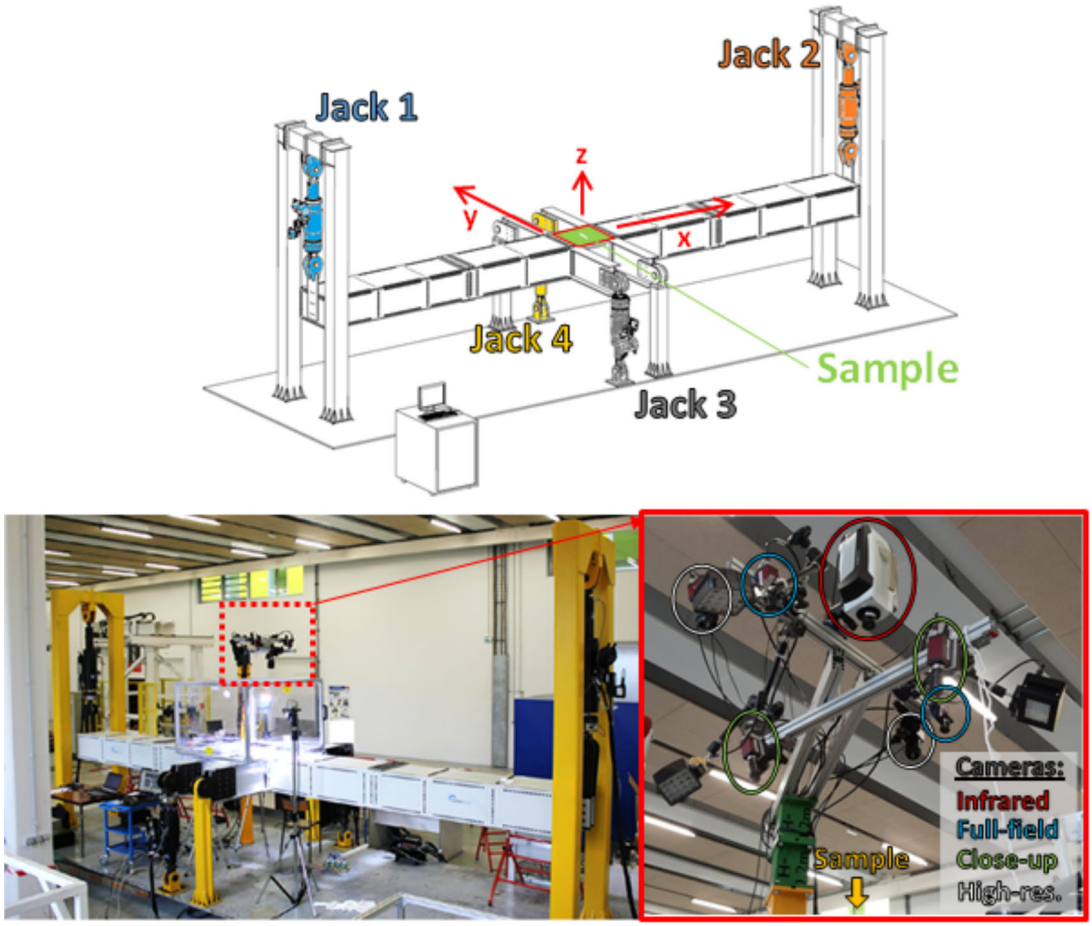

FIGURE 1 Top—schematic diagram of the VERTEX test rig; bottom—photograph of the VERTEX test rig—close-up view on the cameras.

concentration region. The acquisition frequency was set to one frame per second while a test lasts several minutes. The available DIC hardware parameters are summarized in Table 1.

2.2 | Fractal speckle

One of the most important elements in DIC is the pattern deposited on test sample surfaces, as measurement accuracy strongly depends on specific features of this pattern [37]. The International Digital Image Correlation society emphasized the necessity to have a speckle pattern function of the field of view. The first rule of thumb to use is to have a speckle at least 3 pixels in size to avoid aliasing [38]. Complexity arises when several cameras with different resolutions are used to monitor the same specimen. A unique speckle cannot easily be optimized for several image resolutions. Therefore in some works [27], zones with different speckle sizes have been defined. In Figure 3, most of the speckle pattern is adapted to FF cameras that observe the whole plate. For NF cameras, observing crack propagation, the speckle size is much smaller that results in a better measurement accuracy.

However, zones with smaller speckle sizes at the notch tips may turn uniformly grey for FF cameras. This will induce very noisy results. Indeed, the second rule of thumb that is to have 2–3 speckles within a subset [39] would not be respected. Bi-scale patterns have been created so that the full image can be seen simultaneously by two cameras with different resolutions [32]. The limits to this methodology are that there is little chance that just two scales would be enough for industrial structures and that these two particular scales should be known precisely before the beginning of the experiments [40].

A better multiscale pattern is therefore needed. An innovative one based on a fractal (self-affine) surface has recently been developed by Fouque et al. [33]. Details about how to numerically generate this type of pattern from a

14751305, 0, Downloaded from https://onlinelibrary.wiley.com/doi/10.1111/str.12479 by Cochrane France, Wiley Online Library on [23/05/2024]. See the Terms and Conditions (https://onlinelibrary.wiley.com/terms-and-conditions) on Wiley Online Library for rules of use; OA articles are governed by the applicable Creative Commons License

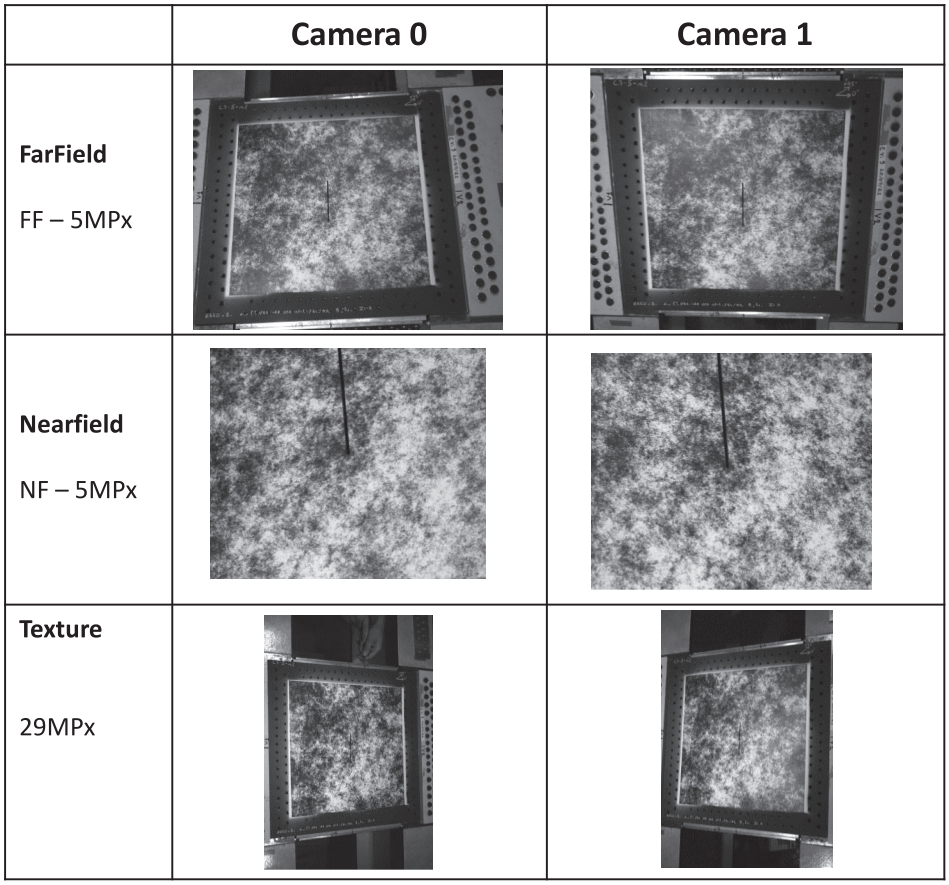

FIGURE 2 Views from the 6 different cameras used on the VERTEX test rig.

TABLE 1 DIC hardware parameters.

Setups	FarField	NearField	Texture
Camera	AVT Pike	AVT Pike	Prosilica GT6600
Resolution	2402 × 2052	2402 × 2052	6576 × 4384
Focal length	16 mm	50 mm	16 mm
Standoff distance	1 m	1 m	1 m
Stereo angle	23.5°	17°	26.3°
Image scale	3.2 pixels/mm	14.1 pixels/mm	7.7 pixels/mm

desired auto-correlation function are available in the aforementioned paper but will not be recalled herein. However, before using this pattern for stereocorrelation purposes, we investigated its grey level conservation properties. Comparisons of the grey level histogram after 5 levels of downscaling have been performed between three types of speckles deposited on top of our large composite specimens (Figure 4): (a) spray paint (manually deposited), (b) printed Perlin noise and (c) printed Fractal. Both prints have been done by the same printer. The Fractal speckle does maintain a largest histogram after several downscaling operations and therefore seems well adapted for our multiscale monitoring of the sample tested on the VERTEX bench.

2.3 | Material and loading

The specimen geometry considered for this study (Figure 2) is a 558 mm * 536 mm flat plate, with 128 holes to bolt the specimen to the test bench, which leaves a 400 mm * 400 mm *gage region*. The plate is a 9-ply composite laminate

14751305, 0, Downloaded from https://onlinelibrary.wiley.com/doi/10.1111/str.12479 by Cochrane France, Wiley Online Library on [23/05/2024]. See the Terms and Conditions (https://onlinelibrary.wiley.com/terms-and-conditions) on Wiley Online Library for rules of use; OA articles are governed by the applicable Creative Commons License

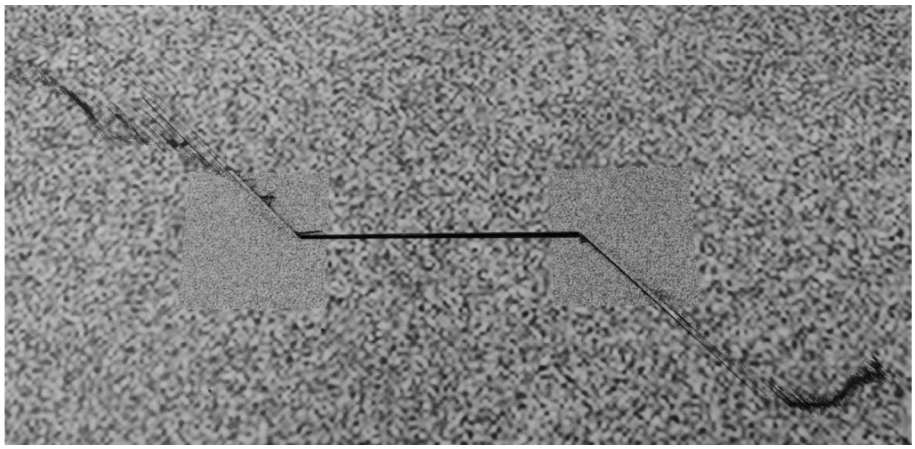

FIGURE 3 Plate from the VERTEX project [34] with two different speckle sizes.

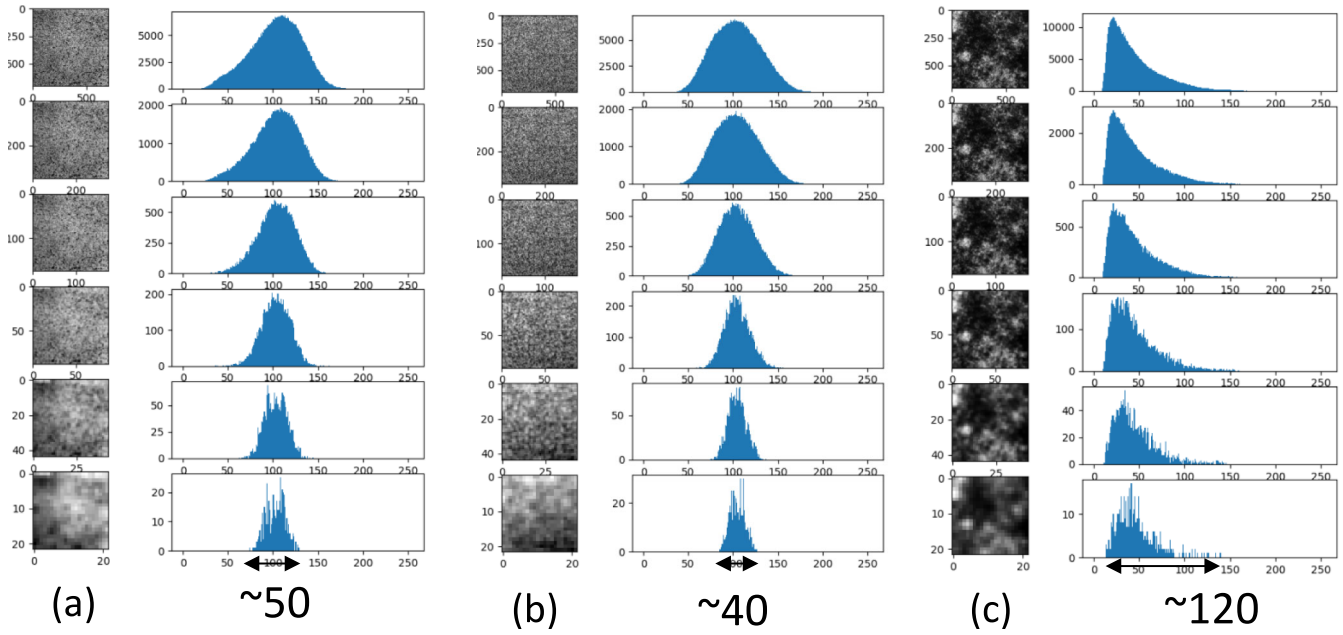

FIGURE 4 Amplitudes of grey levels repartition after 5 levels of downscaling for (a) spray paint—50, (b) printed Perlin—40 and (c) printed Fractal—120.

obtained from carbon/epoxy prepeg plies polymerized in autoclave. The stacking sequence is kept confidential with a total thickness of 1.125 mm. Due to confidentiality issues, material name and parameters cannot be disclosed. A central notch of 100 mm has been milled. A Tension + Shear loading is applied to the specimen until total failure. Jacks 1 and 2 (Figure 1) are used to apply tension in the specimen through bending of the central box. Jacks 3 and 4 are used to apply shear in the specimen through torsion of the central box.

3 | MULTISCALE SDIC

The limited amount of information (1 scalar value per pixel), its quantization (1 integer between 0 and 255) and its discrete repartition (sampling) makes DIC an ill-posed problem. Several approaches to circumvent this issue have been employed. The most common one is to assume the unknown displacement to be continuous over the entire ROI. It is usually sought as a linear combination of a set of shape functions that can be of different types. One convenient choice is offered by meshes used in the FE method because it allows for straightforward connections between experiment and simulation: the same FE mesh used for the displacement field measurement can also be used for numerical analyses.

14751305, 0, Downloaded from https://onlinelibrary.wiley.com/doi/10.1111/str.12479 by Cochrane France, Wiley Online Library on [23/05/2024]. See the Terms and Conditions (https://onlinelibrary.wiley.com/terms-and-conditions) on Wiley Online Library for rules of use; OA articles are governed by the applicable Creative Commons License

3.1 | SDIC

3.1.1 | Calibration

In this work, as 3D displacement measurements were needed, an SDIC method has been used. Recent developments on global approach to SDIC have shown the great adaptability and resilience of the method [16, 27]. Moreover, the FE-SDIC method simplifies the comparison between experimental results and numerical simulation by using FE shape functions as a basis in the measurement algorithm.

Before performing any displacement measurement, one needs to determine the properties of the cameras through a calibration phase. Camera models are an elementary tool in DIC and SDIC enabling a description to be obtained of how a point in the three-dimensional space is captured by a camera in a two-dimensional picture. Figure 5 recalls the main parameters of a pinhole model of a camera.

In order to use the FE geometry and kinematic within the 3D-DIC problem [41], Pierré et al. [27] reformulated the minimisations associated with the method, using the 3D mesh as a support and its associated frame as the world

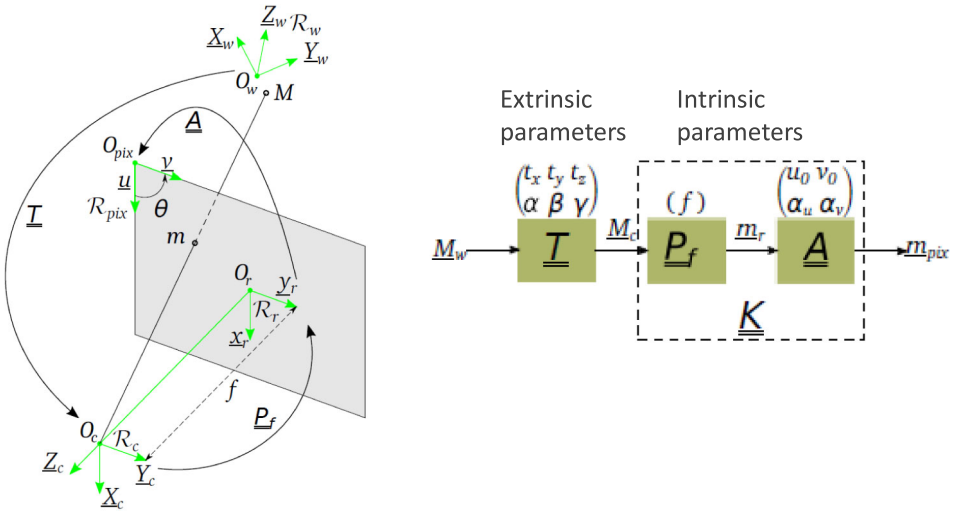

FIGURE 5 Model of one camera going from the world coordinate system (*Rw* in meters) to the image coordinate system (*Rpix* in pixels) using extrinsic and intrinsic parameters [40].

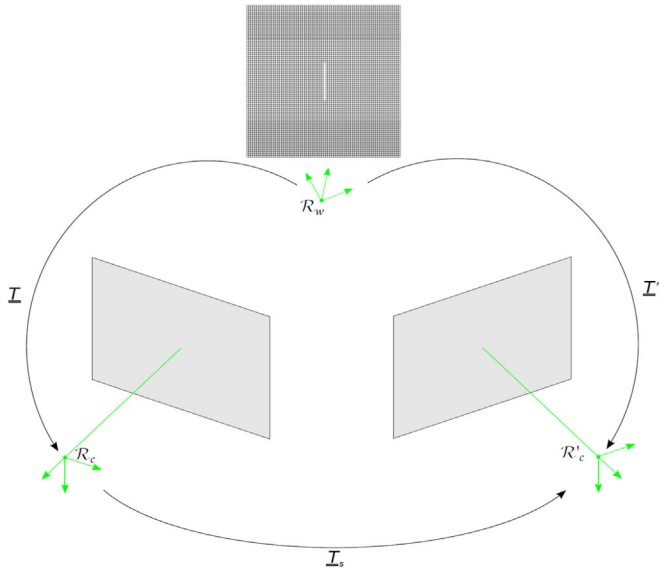

FIGURE 6 Extrinsic parameters for a stereo rig (adapted from Fouque [40]).

14751305, 0, Downloaded from https://onlinelibrary.wiley.com/doi/10.1111/str.12479 by Cochrane France, Wiley Online Library on [23/05/2024]. See the Terms and Conditions (https://onlinelibrary.wiley.com/terms-and-conditions) on Wiley Online Library for rules of use; OA articles are governed by the applicable Creative Commons License

coordinate system. This enables a straightforward dialogue between simulation and DIC. With this methodology, one needs to determine the extrinsic parameters of each camera relative to the mesh reference coordinate (T and T′—Figure 6) whereas numerous commercial correlation software that only use pixel data only need the transformation matrix to go from the reference camera to the other one (Ts—Figure 6).

The classic photogrammetric calibration using targets is enough to both determine the intrinsic parameters of each camera and the transformation matrix to go from the reference camera to the other one. However, to determine the extrinsic parameter of each camera relative to the mesh reference coordinate, an additionnal step is required.

The minimization problem to solve for a stereo rig is the following:

$$p^{0*}, p^{1*} = argmin \int_{\Omega} \left[f^0\left(P^0\left(\boldsymbol{X}, p^0\right)\right) - f^1\left(P^1\left(\boldsymbol{X}, p^1\right)\right)\right]^2 d\boldsymbol{X} \tag{1}$$

with $\boldsymbol{p^c}$ the parameters (intrinsics and extrinsics) of the projector $\boldsymbol{P^c}$ of a given camera and f^0, f^1 the reference images of the camera 0 and 1, respectively. The intrinsics are being fixed for this problem because they have been determined with the calibration target. Only the extrinsics vary. $\boldsymbol{X}$(X,Y,Z) evolves in Ω, the surface mesh. Equation (1) is nonlinear and is solved using a Gauss–Newton algorithm. A good initialization is therefore crucial. One possibility [42] is to identify specific points that can be easily recognized both on the image and on the mesh. Vertices and notch extremities will be used in the present case (Figure 7). The initialization of these parameters is performed for each camera by minimizing the grey level residual between the feature marks (identified on the image) and the projection on the image of the physical positions of the same feature marks (identified on the mesh). It is the same bundle adjustment type problem as for the intrinsic calibration with a calibration target. If this type of initialization is not enough, one can set up an extra step minimizing the distance to feature marks (lines, circles) using level-set methods [42].

The initial shape measurement can be performed using the same formulation as the one described by Equation (1) but with $\boldsymbol{X}$ (X, Y, Z) as the quantity sought. In this case, only the Z coordinate can be modified to avoid convergence issues. As detailed by Colantonio [42], to improve both speed of the algorithm and residuals, an alternate minimization can be processed: one to determine extrinsic parameters and one to determine the initial shape of the specimen.

3.1.2 | Displacement measurement

The FE-SDIC formulation used in this paper can be derived from the minimization of the grey level residual between a reference picture f_{ref} and a deformed picture f_{def}:

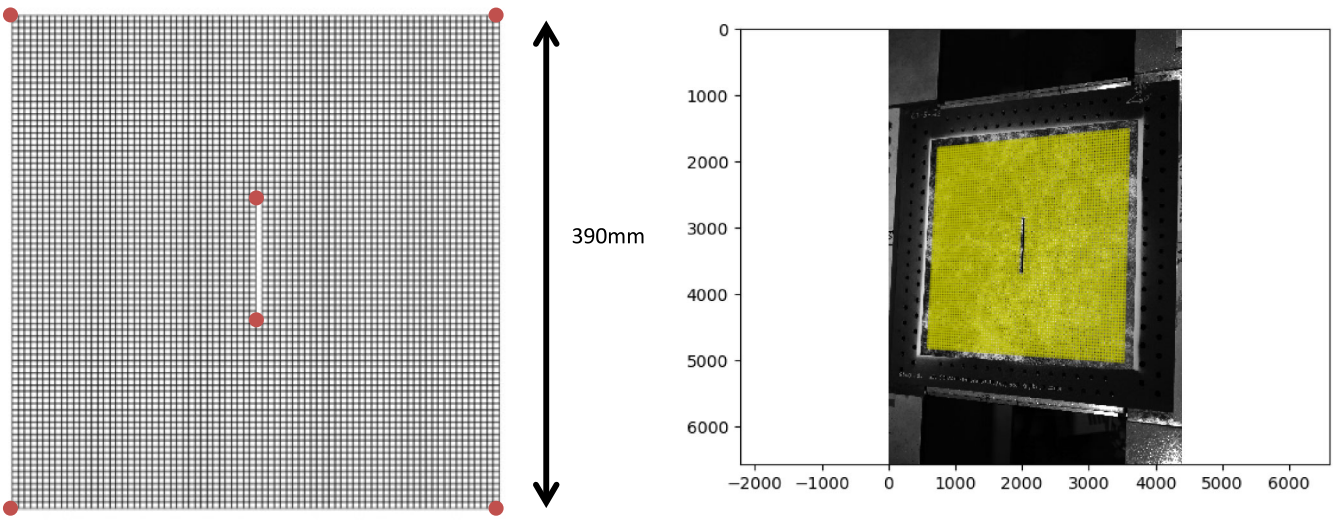

FIGURE 7 Left—mesh used for measurement with feature marks. Right—mesh positioned on the image for the camera 0 (29MPx) after extrinsics calibration.

14751305, 0, Downloaded from https://onlinelibrary.wiley.com/doi/10.1111/str.12479 by Cochrane France, Wiley Online Library on [23/05/2024]. See the Terms and Conditions (https://onlinelibrary.wiley.com/terms-and-conditions) on Wiley Online Library for rules of use; OA articles are governed by the applicable Creative Commons License

$$u^* = argmin \sum_{cam} \int_{\Omega} \left(f_{ref}^{cam}(P^{cam}) - f_{def}^{cam}(u, P^{cam}) \right)^2 \quad (2)$$

with, $\boldsymbol{u}$, the unknown 3D displacement and $\boldsymbol{P^{cam}}$ the projector relating the 3D world coordinates to the 2D pixels of the image. To solve this problem in a finite dimension space, displacement $\boldsymbol{u}$ is chosen to depend on a finite number of parameters $\mathbf{q}$, sometimes referred to as degrees of freedom. A Gauss–Newton scheme is used to minimize the above minimization problem. At iteration k, the linearization around the solution $\boldsymbol{u}$ written as a function of parameters $\mathbf{q}$ [27] leads to

$$\left(\sum_{cam} \mathbf{M}_{dic}^{cam,k} \right) \mathbf{q} = \left(\sum_{cam} \mathbf{b}_{dic}^{cam,k} \right) \quad (3)$$

with $\mathrm{M} = \int_{\Omega} \nabla f_{ref} \frac{\partial u}{\partial q} \times \nabla f_{ref} \frac{\partial u}{\partial q}$; $b = \int_{\Omega} \nabla f_{ref} \frac{\partial u}{\partial q} \times \left(f_{ref} - f_{def} \right)$; and *cam* is the camera's index.

Among the different choices available to describe the displacement u, we chose to use the same FE basis as the one used in the simulations. The elements in this case are shell elements (Q4).

3.2 | A new calibration procedure

Sometimes, natural features such as cracks or edges are not available to help initiate calibration. One way to avoid using artificial markers (embedded in the speckle or not) and have full flexibility regarding the position of the focused area is to capture the 'intrinsic texture' of the specimen offline. For more than 2 cameras, the cost of the minimization (Equation 1) problem to determine extrinsic parameters of all cameras increases quadratically because reference images of all cameras are compared two-by-two. For n cameras, there are $\frac{\mathrm{n(n-1)}}{2}$ couples. Dufour et al. [16] created a reference object $\widehat{f}$ where a texture is created (Equation 4). It is then possible to minimize the grey levels residual between each camera and this object. Therefore, only n couples are to be considered.

$$\widehat{f} = \frac{1}{N_{cam}} \sum_{cam} f_{cam}(P_{cam})) \quad (4)$$

with N_{cam} the total number of cameras.

In the present work, we took inspiration from Dufour et al.'s idea [16] and used the high-resolution cameras (29MPx) to establish a reference 'texture' $\widehat{f}$ defined by the image taken by Camera 1 (Figure 2). This reference texture will be used in the calibration process and will act as a 'virtual' calibration target. A high resolution has been taken for the large field of view to be comparable in terms of resolution with the 5MPx in the focused (NearField) area. It has to be noted that the concept of 'texture' has recently been extended by Fouque et al. within the Photometric DIC framework [43].

The calibration procedure followed is presented in Figure 8, and each step is detailed in the following paragraphs.

3.2.1 | Intrinsics calibration of all cameras

For cameras that have a large field of view ('Texture' and 'FarField'), a large calibration target is used ($6 \times 5 \times 60$ mm). For cameras focused on the side of the notch ('NearField'), a small calibration target is used ($12 \times 9 \times 5$ mm). During the experiments, we used a white blanket to cover the bolt holes of the machine in order to facilitate calibration target circles detection in the images. The methodology presented in Section 3.1.1 was used. For all 6 cameras, the standard deviation between the positions of the calibration target circles detected on the images and calculated from the projectors converged below 0.5 pixels. Calibration residuals are calculated (in pixels) for each camera (0 and 1) and are available in Table 2. For each camera (0 or 1), the value represents the standard deviation of the difference in pixels position of the detected circles centre and the position calculated from the projectors.

14751305, 0, Downloaded from https://onlinelibrary.wiley.com/doi/10.1111/str.12479 by Cochrane France, Wiley Online Library on [23/05/2024]. See the Terms and Conditions (https://onlinelibrary.wiley.com/terms-and-conditions) on Wiley Online Library for rules of use; OA articles are governed by the applicable Creative Commons License

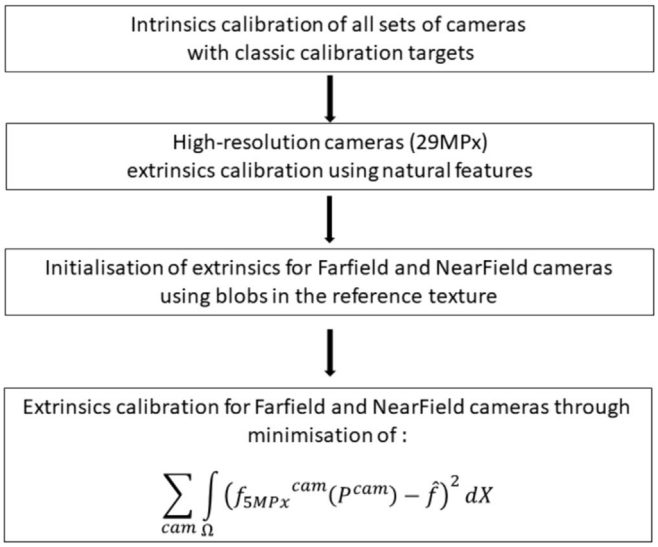

FIGURE 8 Multiscale calibration procedure.

TABLE 2 Calibrations residuals.

	Camera 0	Camera 1
29MPx intrinsics calibration residuals	0.26 pixels	0.29 pixels
29MPx extrinsics calibration residuals	2.30%	
5MPx FF intrinsics calibration residuals	0.35 pixels	0.89 pixels
5MPx FF extrinsics calibration residuals	3.28%	3.66%
5MPx NF intrinsics calibration residuals	0.12 pixels	0.11 pixels
5MPx NF extrinsics calibration residuals	6.88%	6.27%

3.2.2 | High-resolution cameras (29MPx) extrinsics calibration

The extrinsics of the 'texture' cameras have been determined using the methodology described in Section 3.1.1. Six points have been used as feature marks to initialize the parameters values (Figure 7–left). Afterwards, extrinsic parameters have been determined minimizing the difference between images coming from Camera 0 and 1. The output is the mesh correctly positioned in the image (Figure 7—right). In this case, the calibration/shape measurement phase is considered correctly converged when the standard deviation of the grey level difference between the images from Cameras 0 and 1 goes below 2% of the dynamic (average of the grey level amplitudes). Calibration residuals are calculated (in % of the image dynamic) and are presented in Table 2. The value represents the standard deviation of the difference in pixel level determined at the projected positions of the Integration Points in the left (camera 0) and right (camera 1) reference images.

3.2.3 | FF and NF cameras (5MPx) extrinsics calibration

Identical procedures have been used for both FF and NF rigs (both cameras 0 and 1). The first step is to initialize extrinsics with feature marks that will be created from the speckle paint itself. Blobs are detected in the high-resolution camera (top left—Figure 9) and in the camera we want to calibrate (top right—Figure 9) using the SIFT algorithm. SIFT is a scale invariant template matching technique. It means that it can recognize features or fiducials even if they are rotated or scaled. Thanks to this property, SIFT is usually used to help grey level-based registration techniques when initialization in challenging, for instance in multiscale framework [12] or in large deformations/rotations [28].

Second, each blob of the first set (high-resolution camera) is tested against the second set (camera to calibrate) using the results of an intercorrelation of windows around blobs. When the images are of different resolution (29Mpx of

14751305, 0, Downloaded from https://onlinelibrary.wiley.com/doi/10.1111/str.12479 by Cochrane France, Wiley Online Library on [23/05/2024]. See the Terms and Conditions (https://onlinelibrary.wiley.com/terms-and-conditions) on Wiley Online Library for rules of use; OA articles are governed by the applicable Creative Commons License

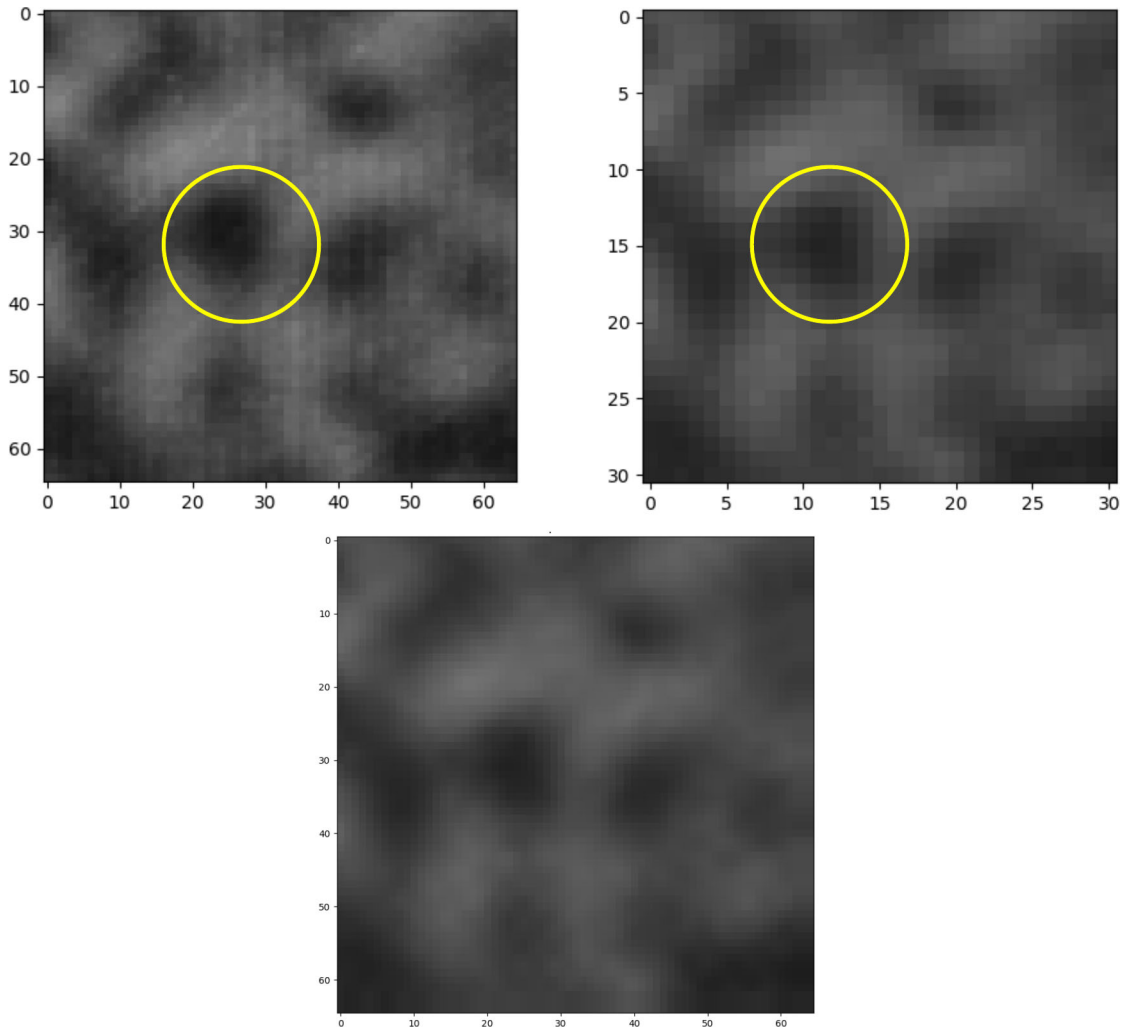

FIGURE 9 Top left—blob detected in the 29MPx image; top right—blob detected in the 5MPx image; bottom—window of correlation (5MPx) interpolated on a 29MPx resolution.

texture camera and 5MPx of Farfield camera), the image of the lower resolution is interpolated using B-splines (bottom—Figure 9). The common blobs in both images will serve as keypoints (Figure 10). Calibration residuals are calculated (in % of the image dynamic) for each camera (0 and 1) and are available in Table 2. For each camera, the value represents the standard deviation of the difference in pixels levels determined at the projected positions of the Integration Points in the reference images of the camera to calibrate and the HR camera (texture).

Keypoints coordinates in the images are then identified (u_{k5}, v_{k5}) in the 5MPx images and (u_{k29}, v_{k29}) in the 29MPx images. As the high-resolution cameras are fully calibrated, the coordinates of the Integration Points $(x_{k29},y_{k29},z_{k29})$ whose projection in the images is the closest to the keypoints detected (u_{k29}, v_{k29}) can be determined. Instead of determining these coordinates using an inverse projection, this approximation simplifies the algorithm with an acceptable accuracy (<0.5 pixels). The extrinsics of both NF and FF cameras are then initialized by minimizing the residual between the keypoints coordinates in the images (u_{k5},v_{k5}) and the projection of the coordinates of the Integration Points $[(x_{k5},y_{k5},z_{k5}) = (x_{k29},y_{k29},z_{k29})]$. It must be noted that a minimum number of 3 keypoints were required to initialize the calibration of extrinsic parameters. Moreover, even though a qualitative study has not been undertaken in the present work, the more the keypoints used are distant, the smaller are the correlation residuals (after the initialization phase). The keypoints are only used as an initialization for the actual calibration algorithm that uses a global grey level formulation and thus relies on all (as many as possible) pixels in the ROI. As such, the accuracy required is limited to bringing the parameters sufficiently close to the solution to make the following minimization algorithm converge (Equation 5).

14751305, 0, Downloaded from https://onlinelibrary.wiley.com/doi/10.1111/str.12479 by Cochrane France, Wiley Online Library on [23/05/2024]. See the Terms and Conditions (https://onlinelibrary.wiley.com/terms-and-conditions) on Wiley Online Library for rules of use; OA articles are governed by the applicable Creative Commons License

$$\sum_{cam} \int_{\Omega} \left(f^{cam}_{5MPx}(P^{cam}) - \widehat{f} \right)^2 dX \tag{5}$$

In the present case, the number of 5MPx cameras is 4 (Camera 0 and 1 for NF and FF). This procedure defines integration points in the HR image (29MPx). Therefore, a pixel in a 5MPx camera might (and most probably will) contains several projections of these integration points due to the difference between the resolution of the images. However, these discrepancies do not impact the methodology significantly.

The residual maps (in % of the dynamic) before and after the minimization of Equation (3) are displayed in Figure 11 for the FF (Camera 0). Similar behaviour has been observed for the other FF cameras as well as for NF ones. A graphic output of this extrinsics calibration phase is the positioning of the projection of the mesh in the image. Figure 12 (top) displays it for Camera 0 of the NF system.

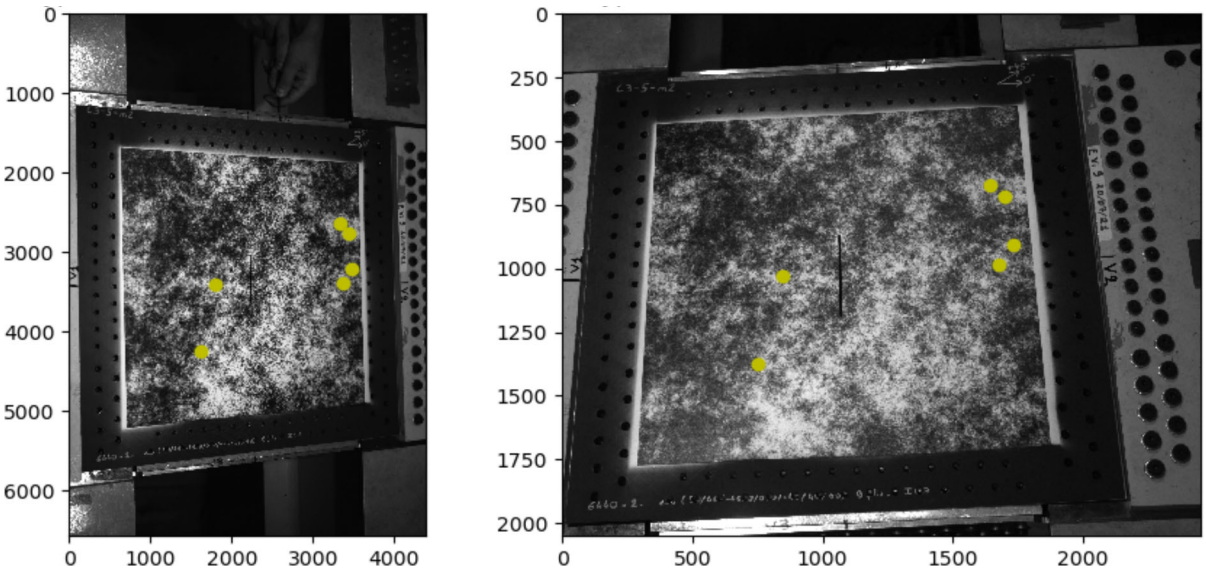

FIGURE 10 Blobs detected in the 29MPx image (left) and 5MPx image (right).

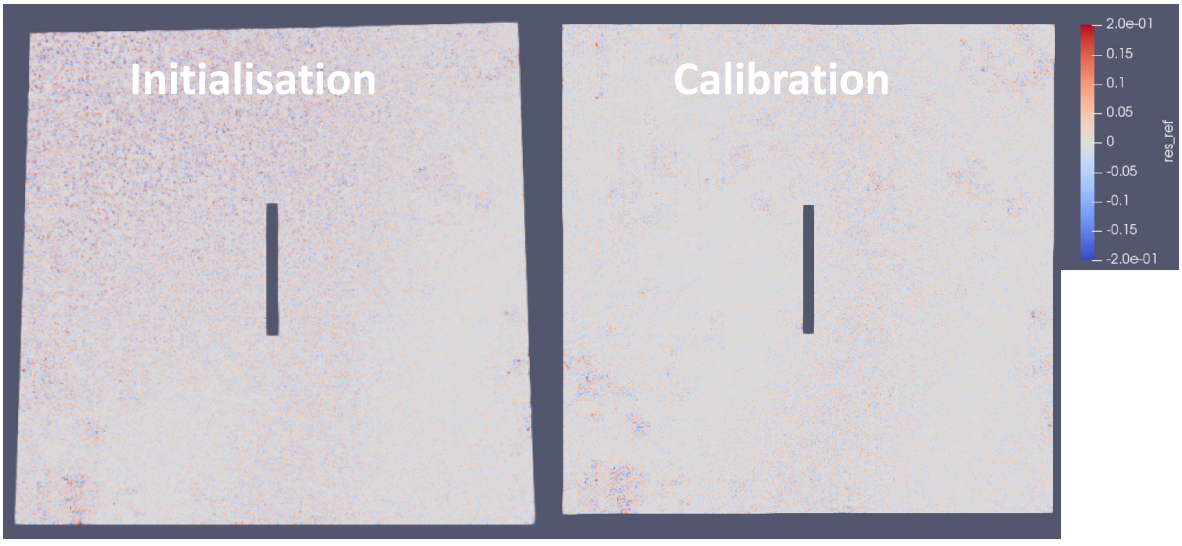

FIGURE 11 Residual map between 5MPx FF and 29MPx images from Camera 0 (% of the dynamic).

14751305, 0, Downloaded from https://onlinelibrary.wiley.com/doi/10.1111/str.12479 by Cochrane France, Wiley Online Library on [23/05/2024]. See the Terms and Conditions (https://onlinelibrary.wiley.com/terms-and-conditions) on Wiley Online Library for rules of use; OA articles are governed by the applicable Creative Commons License

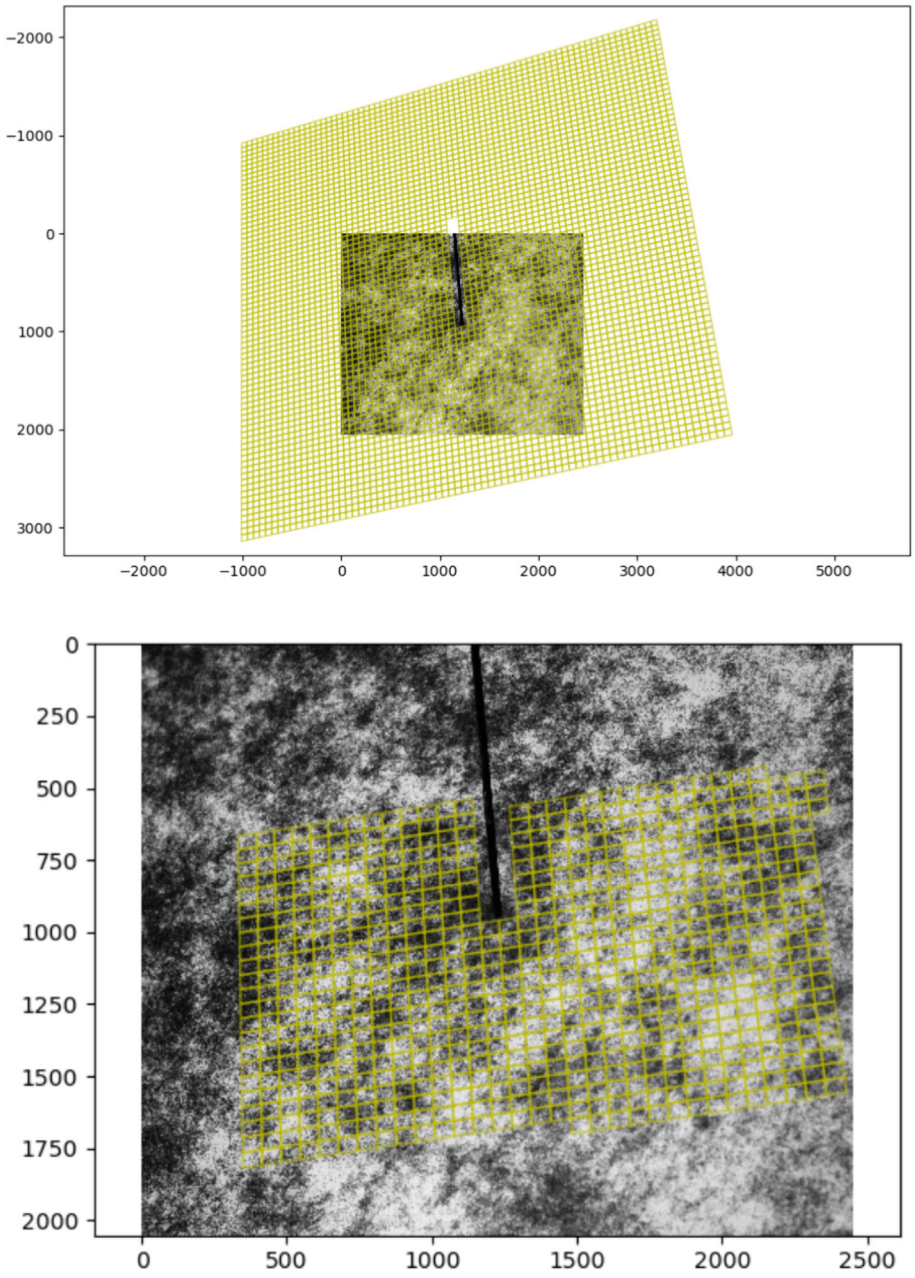

FIGURE 12 Top—mesh positioned on the image for the camera 0 (5MPx—NearField) after extrinsics calibration; bottom—partition of the mesh used for NearField measurement.

3.3 | A new displacement measurement

3.3.1 | Classic mesh

Multiscale advantage is to be able to benefit both from a large field of view (5MPx—FF) and a focused field of view in the zone of interest (5MPx—NF). One solution would consist in performing measurement with NF cameras with the mesh associated (Figure 12—bottom) on one hand and FF cameras with the mesh associated (Figure 7—right) on the other hand and to manually replace the displacement measured by the NF cameras in the zone near the notch in the global mesh. To avoid the hassle, the authors present here a way of merging the data from NF and FF cameras.

14751305, 0, Downloaded from https://onlinelibrary.wiley.com/doi/10.1111/str.12479 by Cochrane France, Wiley Online Library on [23/05/2024]. See the Terms and Conditions (https://onlinelibrary.wiley.com/terms-and-conditions) on Wiley Online Library for rules of use; OA articles are governed by the applicable Creative Commons License

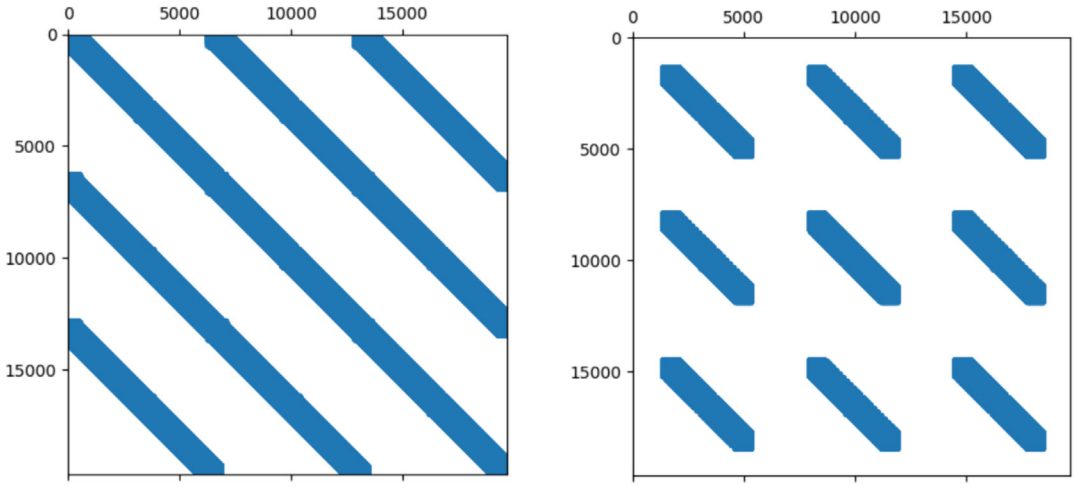

FIGURE 13 Left: sparse matrix $M_{dic}^{cam\ Farfield}$; right: sparse matrix $M_{dic}^{cam\ Nearfield}$.

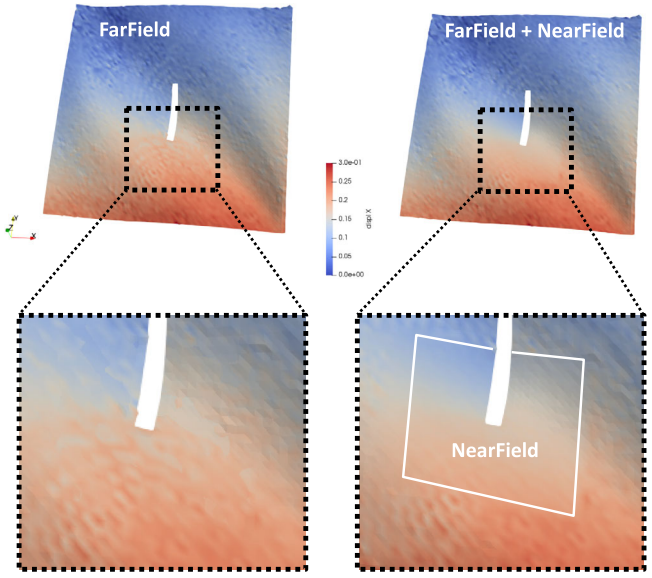

FIGURE 14 Displacement (×20) along X axis focused in a zone around the notch—just before first failure. Left—measurement from 5MPx FF; right—measurement from 5MPx FF + NF.

The degree of freedoms numbering and the connectivity of the global mesh are kept for the local mesh. From Equation (3), one can define $\mathbf{M}_{dic}^{cam\ Farfield}$, $\mathbf{M}_{dic}^{cam\ Nearfield}$, $\mathbf{b}_{dic}^{cam\ Farfield}$ and $\mathbf{b}_{dic}^{cam\ Nearfield}$ such that at iteration k of the Gauss–Newton solver becomes as follows:

$$\left(\sum_{cam\ Farfield}\mathbf{M}_{dic}^{cam\ Farfield,k}+\sum_{cam\ Nearfield}\mathbf{M}_{dic}^{cam\ Nearfield,k}\right)\mathbf{q}=\sum_{cam\ Farfield}\mathbf{b}_{dic}^{cam\ Farfield,k}+\sum_{cam\ Nearfield}\mathbf{b}_{dic}^{cam\ Nearfield,k} \tag{6}$$

The sparse matrix $\mathbf{M}_{dic}^{cam\ Nearfield}$ therefore contains many zeros compared to the sparse matrix $\mathbf{M}_{dic}^{cam\ Farfield}$ (Figure 13).

Figure 14 outputs the displacement along X axis just before the first damage occurs. The left part of the image has been obtained through stereo DIC using only the FF cameras. The right part of the image has been obtained through stereo DIC using both FF and NF cameras with the formulation described in Equation 6. It is very clear when comparing the zoomed area around the notch that the additional data from the NF cameras enriched the measurement. One

14751305, 0, Downloaded from https://onlinelibrary.wiley.com/doi/10.1111/str.12479 by Cochrane France, Wiley Online Library on [23/05/2024]. See the Terms and Conditions (https://onlinelibrary.wiley.com/terms-and-conditions) on Wiley Online Library for rules of use; OA articles are governed by the applicable Creative Commons License

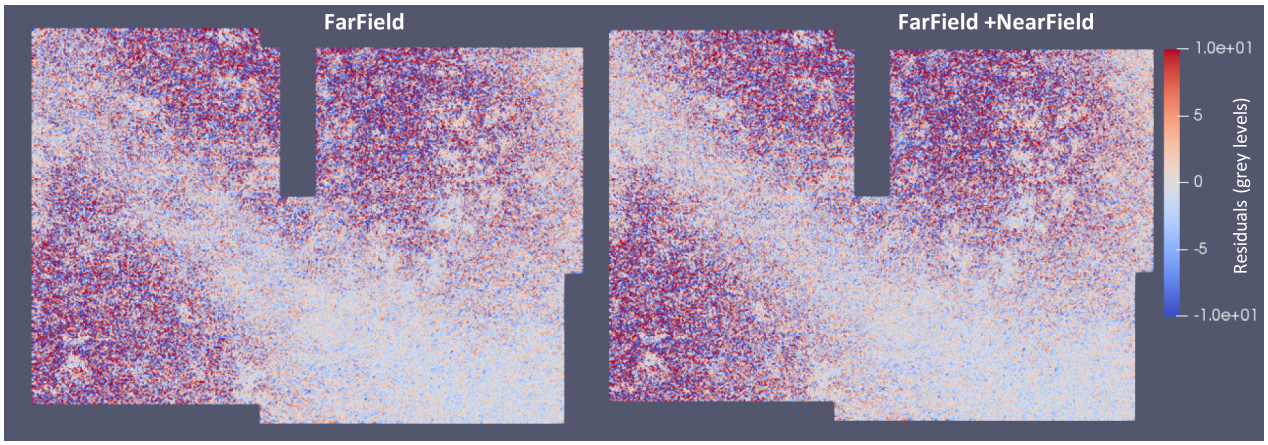

FIGURE 15 Residuals in grey levels using NF images (just before failure and reference one) of camera 0: left—using displacement calculated from FF images only; right—using displacement calculated from FF and NF images

TABLE 3 DIC analysis parameters used for the correlation.

Setups	FarField	NearField + FarField
DIC software	Pyxel	Pyxel
Image filtering	Blur 1px	Blur 1px
Element size	5 mm * 5 mm	5 mm * 5 mm (FF) 2.5 mm × 2.5 mm (NF)
Element type	Q4	Q4
Interpolant	Cubic spline	Cubic spline

can notice that the displacement variation is a lot smoother as well as the notch contour. Moreover, residuals (in grey levels) have been determined using NF images (camera 0) and displayed on the partition of the mesh near the notch in Figure 15. Two configurations have been studied: one with the displacements determined using only the FF images (left) and the other one with the displacements determined using both data from FF and NF images (Equation 6). One can notice a small reduction of the residuals with the new displacement measurement (NF + FF). The same methodology has been followed on the global mesh and using FF images, and similar results have been obtained regarding the residuals. The standard deviation obtained was 1.82% (of the dynamic of the image) regardless of the use of NF images. This can be explained by an improvement obtained on the displacement field (Figure 14) that is too small to be detected when calculating the residuals on images with 'big pixels' (FF).

The DIC analysis parameters used for the correlation are summarized in Table 3.

3.3.2 | Refined mesh

Usually in DIC, the question of the FE measurement mesh size always involves a trade-off. Indeed, the 'True Error' is a combination of 'systematic error' (FE error) that rises linearly with the size of the element and 'random error' (DIC error) that is inversely proportional to number of pixels in the element (therefore to the size of the element). The objective of multiscale measurement is to locally add pixels in areas where smaller FEs are needed for a better description of the kinematic fields. The Fractal-type speckle pattern we used is perfectly adequate for this configuration, as detailed in Section 2.2. Measurement has been performed with a refined mesh around the notch as displayed in Figure 16. The results are extremely similar to the one obtained with the uniform mesh. One can distinguish a bit more noise on displacements for the refined mesh configuration when they are scaled 50 times (Figure 16). In other words, refined mesh results are consistent since the speckle pattern remained unchanged and the size of the elements decreased. To take full advantage of this refined pattern, future work is planned to perform correlation after the first crack propagation.

14751305, 0, Downloaded from https://onlinelibrary.wiley.com/doi/10.1111/str.12479 by Cochrane France, Wiley Online Library on [23/05/2024]. See the Terms and Conditions (https://onlinelibrary.wiley.com/terms-and-conditions) on Wiley Online Library for rules of use; OA articles are governed by the applicable Creative Commons License

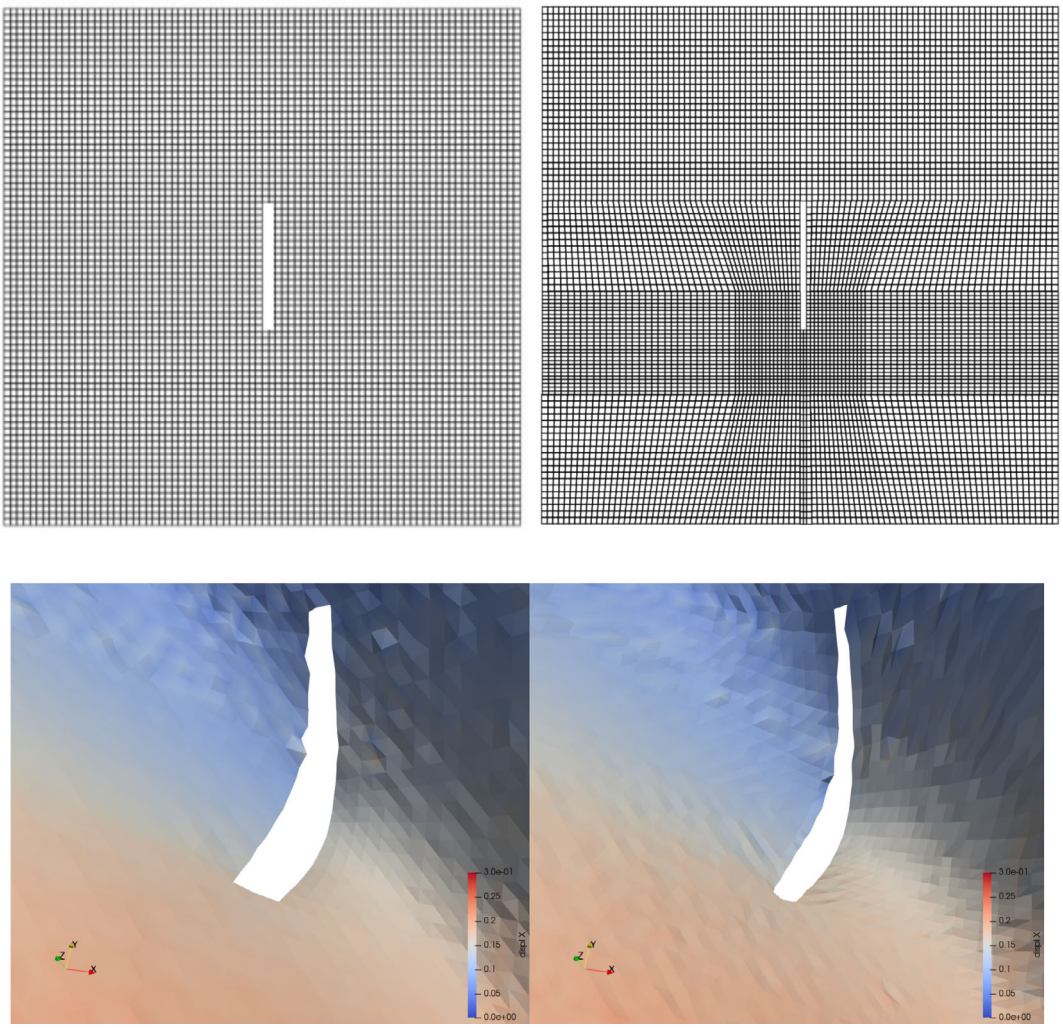

FIGURE 16 Displacement (×50 times) along X axis focused in a zone around the notch—just before first failure. Left—measurement from Farfield + NearField *Uniform* mesh; right—measurement from Farfield + NearField *Refined* mesh.

4 | CONCLUSIONS

A 6-camera system has been developed to measure the 3D displacement field of a notched composite laminate subjected to a biaxial loading. The goal is to obtain data both at the boundaries of the specimen (to provide regularized boundary conditions for numerical models) and around the notch (where higher displacement gradients are expected and should be captured). Therefore, two 5MPx cameras were selected to monitor the specimen with a wide field of view and a second pair for displacement measurements around the notch to take advantage of higher resolution. In order to avoid aliasing problems that often arise when using different cameras resolution, a Fractal-type speckle pattern [33] was adopted. The latter can be used over a very wide range of resolutions because the recorded grey distribution does not shrink much when downscaled.

Two high-resolution cameras (29MPx) were used prior to the test to create an 'intrinsic texture' that will help calibrate the FF and NF camera systems without the use of external feature marks. The 'texture' cameras are classically calibrated, then common features are detected between 5MPx images and 29MPx images, and eventually, a bundle-type adjustment method is used to initiate the calibration. Minimization is sought between each camera and the 'intrinsic texture' as opposed to the traditional formulation that compares each possible pair of cameras. Low correlation residuals demonstrate the quality of this methodology.

Our approach does not require any 3D stitching operations because the multi-camera system provides all the 3D measurements directly in a common coordinate system. A step forward has been made by merging data from the NF measurement into the FF measurement. The results in terms of displacement fields clearly outline a benefit (less noise)

14751305, 0, Downloaded from https://onlinelibrary.wiley.com/doi/10.1111/str.12479 by Cochrane France, Wiley Online Library on [23/05/2024]. See the Terms and Conditions (https://onlinelibrary.wiley.com/terms-and-conditions) on Wiley Online Library for rules of use; OA articles are governed by the applicable Creative Commons License

in the enriched zone (more information per element). A first attempt was made with a refined mesh around the notch. The speckle pattern is still valid for smaller elements due to its fractal properties, and enough pixels per element are available with the NF data input. The results are consistent and pave the way for numerous work prospects such as enhanced identification methods (using for example rich strain fields around a notch) and validation of failure simulation models around defects.

ACKNOWLEDGEMENTS

This work has been funded by the 'Fondation Jean-Jacques et Felicia Lopez-Loreta pour l'Excellence Académique' as part of the VIRTUOSE (**VIRT**ual testing of aer**O**nautical **S**tructur**E**s) project (https://websites.isae-supaero.fr/virtuose/).

DATA AVAILABILITY STATEMENT

Data are available on request from the authors.

ORCID

J. Serra https://orcid.org/0000-0002-2466-7673

REFERENCES

[1] D. Gay, S. V. Hoa, S. W. Tsai, *Composite materials: design and applications*, CRC Press, Boca Raton **2002**.
[2] J. Rouchon, 'Certification of large airplane composite structures, recent Progress and new trends in compliance philosophy', presented at the ICAS, 1990. Accessed: Jan. 11, 2022. [Online]. Available: https://www.icas.org/ICAS_ARCHIVE/ICAS1990/ICAS-90-1.8.1.pdf
[3] T. Bru, 'Material characterisation for crash modelling of composites [PhD thesis]', **2018**. https://doi.org/10.13140/RG.2.2.10536.01280
[4] B. Castanié, *Exp. Mech.* **2004**, *44*(5), 461. https://doi.org/10.1177/0014485104047607
[5] A. E. Lovejoy, N. W. Gardner, D. Dawicke, C. V. Jutte, B. D. Smith, Improving Structural Test and Analysis Correlation Using Digital Image Correlation Boundary Measurements, in AIAA Scitech *2020 Forum*, American Institute of Aeronautics and Astronautics, Orlando, FL **2020**.
[6] R. Janeliukstis, X. Chen, *Compos. Struct.* **2021**, *271*, 114143. https://doi.org/10.1016/j.compstruct.2021.114143
[7] B. LeBlanc, C. Niezrecki, P. Avitabile, J. Chen, J. Sherwood, *Struct. Health Monit.* **2013**, *12*(5–6), 430. https://doi.org/10.1177/1475921713506766
[8] N. W. Gardner, M. W. Hilburger, W. T. Haynie, M. C. Lindell, W. A. Waters, *Digital image correlation data processing and analysis techniques to enhance test data assessment and improve structural simulations*, American Institute of Aeronautics and Astronautics **2018**. https://ntrs.nasa.gov/api/citations/20180006177/downloads/20180006177.pdf
[9] K. Patil, V. Srivastava, J. Baqersad, *Measurement* **2018**, *122*, 358. https://doi.org/10.1016/j.measurement.2018.02.059
[10] Z. Wang, H. Li, J. Tong, M. Shen, F. Aymerich, P. Priolo, *Compos. Sci. Technol.* **2008**, *68*(9), 1975. https://doi.org/10.1016/j.compscitech.2007.04.026
[11] J. Carroll, C. Efstathiou, J. Lambros, H. Sehitoglu, B. Hauber, S. Spottswood, R. Chona, *Eng. Fract. Mech.* **2009**, *76*(15), 2384. https://doi.org/10.1016/j.engfracmech.2009.08.002
[12] J.-C. Passieux, F. Bugarin, C. David, J.-N. Périé, L. Robert, *Exp. Mech.* **2015**, *55*(1), 121. https://doi.org/10.1007/s11340-014-9872-4
[13] D. Solav, K. M. Moerman, A. M. Jaeger, K. Genovese, H. M. Herr, *IEEE Access* **2018**, *6*, 30520. https://doi.org/10.1109/ACCESS.2018.2843725
[14] M. Bornert, F. Valès, H. Gharbi, D. Nguyen Minh, *Strain* **2010**, *46*(1), 33. https://doi.org/10.1111/j.1475-1305.2008.00590.x
[15] J. Serra, J. E. Pierré, J. C. Passieux, J. N. Périé, C. Bouvet, B. Castanié, C. Petiot, *Compos. Struct.* **2017**, *180*, 550. https://doi.org/10.1016/j.compstruct.2017.08.055
[16] J.-E. Dufour, F. Hild, S. Roux, *J. Strain Anal. Eng. Des.* **2015**, *50*(7), 470. https://doi.org/10.1177/0309324715592530
[17] X. Shao, Z. Chen, X. Dai, X. He, *Rev. Sci. Instrum.* **2018**, *89*(10), 105110. https://doi.org/10.1063/1.5050187
[18] Z. Li, L. Zhou, H. Lei, Y. Pei, *Compos. Part B Eng.* **2019**, *161*, 87. https://doi.org/10.1016/j.compositesb.2018.10.058
[19] X. Yuan, L. Fang, Q. Dai, D. J. Brady, Y. Liu, *Multiscale gigapixel video: a cross resolution image matching and warping approach*, IEEE **2017** 1. https://drive.google.com/file/d/1otSTAXoiYJGnb71k7clsSQ7F9I80iYEd/view
[20] D. G. Lowe, *Int. J. Comput. Vis.* **2004**, *60*(2), 91. https://doi.org/10.1023/B:VISI.0000029664.99615.94
[21] H. Bay, T. Tuytelaars, L. Van Gool, SURF: Speeded Up Robust Features, in Computer vision – ECCV *2006*, (Eds: A. Leonardis, H. Bischof, A. Pinz) Vol. 3951, Springer Berlin Heidelberg, Berlin, Heidelberg **2006** 404.
[22] B. Triggs, P. F. McLauchlan, R. I. Hartley, A. W. Fitzgibbon, Bundle Adjustment — A Modern Synthesis, in *Vision Algorithms: Theory and Practice*, (Eds: B. Triggs, A. Zisserman, R. Szeliski) Vol. 1883, Springer Berlin Heidelberg, Berlin, Heidelberg **2000** 298.
[23] M. Sutton, W. Wolters, W. Peters, W. Ranson, S. McNeill, *Image vis. Comput.* **1983**, *1*(3), 133. https://doi.org/10.1016/0262-8856(83)90064-1
[24] J. Harvent, Mesure de formes par corrélation multi-images: application à l'inspection de pièces aéronautiques à l'aide d'un système multi-caméras, 171.

14751305, 0, Downloaded from https://onlinelibrary.wiley.com/doi/10.1111/str.12479 by Cochrane France, Wiley Online Library on [23/05/2024]. See the Terms and Conditions (https://onlinelibrary.wiley.com/terms-and-conditions) on Wiley Online Library for rules of use; OA articles are governed by the applicable Creative Commons License

[25] *Correlated solutions, 'VIC-3D-8-manual'*. **2021**. https://correlated.kayako.com/article/57-vic-3d-8-manual-and-testing-guide
[26] Y. Wang, P. Lava, S. Coppieters, P. V. Houtte, D. Debruyne, *Strain* **2013**, *49*(2), 190. https://doi.org/10.1111/str.12027
[27] J.-E. Pierré, J.-C. Passieux, J.-N. Périé, *Exp. Mech.* **2017**, *57*(3), 443. https://doi.org/10.1007/s11340-016-0246-y
[28] K. Genovese, D. Sorgente, *Opt. Lasers Eng.* **2018**, *104*, 159. https://doi.org/10.1016/j.optlaseng.2017.06.020
[29] Y. Sun, J. H. L. Pang, C. K. Wong, F. Su, *Appl. Optim.* **2005**, *44*(34), 7357. https://doi.org/10.1364/AO.44.007357
[30] R. Bouclier, J.-C. Passieux, *Internat. J. Numer. Methods Engrg.* **2017**, *111*(2), 123. https://doi.org/10.1002/nme.5456
[31] E. Jones, M. A. Iadicola, *A good practices guide for digital image correlation*, International Digital Image Correlation Society **2018**. https://idics.org/guide/DICGoodPracticesGuide_PrintVersion-V5h-181024.pdf
[32] G. F. Bomarito, J. D. Hochhalter, T. J. Ruggles, *Exp. Mech.* **2018**, *58*(7), 1169. https://doi.org/10.1007/s11340-017-0348-1
[33] R. Fouque, R. Bouclier, J.-C. Passieux, J.-N. Périé, *Exp. Mech.* **2021**, *61*(3), 483. https://doi.org/10.1007/s11340-020-00649-7
[34] J. Serra, J. E. Pierré, J. C. Passieux, J. N. Périé, C. Bouvet, B. Castanié, *Compos. Struct.* **2017**, *179*, 224. https://doi.org/10.1016/j.compstruct.2017.07.080
[35] A. Trellu, G. Pichon, C. Bouvet, S. Rivallant, B. Castanié, J. Serra, L. Ratsifandrihana, *Compos. Sci. Technol.* **2020**, *196*, 108194. https://doi.org/10.1016/j.compscitech.2020.108194
[36] J. Serra, A. Trellu, C. Bouvet, S. Rivallant, B. Castanié, L. Ratsifandrihana, *Compos. Part C Open Access* **2021**, *6*, 100203. https://doi.org/10.1016/j.jcomc.2021.100203
[37] B. Pan, K. Qian, H. Xie, A. Asundi, *Meas. Sci. Technol.* **2009**, *20*(6), 062001. https://doi.org/10.1088/0957-0233/20/6/062001
[38] P. Reu, *Exp. Tech.* **2014**, *38*(5), 1. https://doi.org/10.1111/ext.12111
[39] P. Reu, *Exp. Tech.* **2014**, *38*(6), 1. https://doi.org/10.1111/ext.12110
[40] R. Fouque, General multiview stereo digital image correlation formulation: towards multiscale digital twins of complex experimental setups, 195.
[41] J. Réthoré, T. Muhibullah, M. Elguedj, P. C. Coret, A. Combescure, *Internat. J. Solids Structures* **2013**, *50*(1), 73. https://doi.org/10.1016/j.ijsolstr.2012.09.002
[42] G. Colantonio, Stéréo-corrélation d'images numériques éléments finis: de l'étalonnage à l'identification, 224.
[43] R. Fouque, R. Bouclier, J.-C. Passieux, J.-N. Périé, *J. Theor. Comput. Appl. Mech.* **2022**. https://doi.org/10.46298/jtcam.7467

How to cite this article: J. Serra, R. Lalanne, J.-E. Dufour, J.-N. Périé, J.-C. Passieux, *Strain* **2024**, e12479. https://doi.org/10.1111/str.12479

14751305, 0, Downloaded from https://onlinelibrary.wiley.com/doi/10.1111/str.12479 by Cochrane France, Wiley Online Library on [23/05/2024]. See the Terms and Conditions (https://onlinelibrary.wiley.com/terms-and-conditions) on Wiley Online Library for rules of use; OA articles are governed by the applicable Creative Commons License